Water Research 223 (2022) 119015

Contents lists available at ScienceDirect

Water Research

journal homepage: www.elsevier.com/locate/watres

Preferential interactions of surface-bound engineered single stranded DNA with highly aromatic natural organic matter: Mechanistic insights and implications for optimizing practical aquatic applications

Bo Peng [a], Peng Liao [b], Yi Jiang [a,*]

[a] Department of Civil and Environmental Engineering, The Hong Kong Polytechnic University, Kowloon, Hong Kong, China
[b] State Key Laboratory of Environmental Geochemistry, Institute of Geochemistry, Chinese Academy of Sciences, 99 Lingcheng West Road, Guiyang 550081, China

ARTICLE INFO

Keywords:
DNA
Natural organic matter
Adsorption
Aromaticity
Divalent cation bridging

ABSTRACT

Engineered short-chain single stranded DNA (ssDNA) are emerging materials with various environmental applications, such as aptasensor, selective adsorbent, and hydrological tracer. However, the lack of fundamental understanding on the interactions of such materials with natural organic matter (NOM) hinders the improvement of their application performance in terms of sensitivity, selectivity, and stability. In this study, we investigated the interactions of ssDNA (four strands with systematically varied length and sequence) with two humic acids (Suwannee River humic acid (SRHA) and Aldrich humic acid (AHA)) and two humic-like NOM present in local aquatic matrices (ROM in river water and WOM in wastewater). Detailed, molecular level interaction mechanisms were obtained by probing the colloidal stability of the ssDNA-coated gold nanoparticles, coupled with product characterization using a suite of microscopic and spectroscopic techniques. Our study revealed that π-π interactions and divalent cation bridging were the major mechanisms for ssDNA-NOM interactions. ssDNA preferentially interacted with NOM with high aromaticity (AHA > SRHA/WOM/ROM). With divalent cations present (especially Ca^{2+}), even a small amount of AHA could completely shield ssDNA, whereas the extent of shielding by SRHA/WOM/ROM depended on the relative content of ssDNA and NOM and whether bridges formed. The extent of shielding of ssDNA by NOM provides a potential answer to the reported conflicting effects of natural water matrices on the performance of DNA-based sensors. Taken together, our findings provide insights into the transformations of engineered ssDNA under environmentally relevant conditions as well as implications for their performance optimization in practical aquatic applications (e.g., from DNA design to pretreatment strategy).

1. Introduction

Engineered DNA strands with desired sequences and a wide range of useful modifications, such as fluorescent tags and linkage molecules, can now be synthesized/purchased at low (and decreasing) costs. The DNA consists of nucleotides in a specific order, and each nucleotide contains a deoxyribose sugar, a phosphate group, and one of the four nitrogenous bases, namely adenine (A), thymine (T), cytosine (C), and guanine (G). They are unique from other synthetic polymers due to their intrinsic functions or embedded information. For example, a short-chain single-stranded DNA (ssDNA) aptamer binds targets with high sensitivity and selectivity, being very promising for rapid, point-of-use, multiplex environmental sensing of organic contaminants (Akki et al., 2015; Fan et al., 2014), ions (Qing et al., 2017), and pathogens (Yu et al., 2018), etc. Aptasensors have the potential to rival some state-of-the-art chemical/biological analytical methods. Also, DNA aptamer has been demonstrated as a highly selective adsorbent to remove arsenic (Kim et al., 2009) and illicit pharmaceuticals (Hu et al., 2011). Engineered DNA with programmed information (i.e., the sequence of nucleotides) can also be used as a tracer to track the source and migration pathways of pollutants in hydrological environment investigations (Liao et al., 2018). The number of DNA tracer is theoretically unlimited (i.e., the combination of four nucleobases) and the unique sequence of each DNA tracer makes it easily distinguishable from environmental background and allows for multipoint tracing.

While the potential of engineered DNA in aquatic applications has

* Corresponding author.
E-mail address: yi-cee.jiang@polyu.edu.hk (Y. Jiang).

https://doi.org/10.1016/j.watres.2022.119015
Received 30 May 2022; Received in revised form 27 July 2022; Accepted 22 August 2022
Available online 23 August 2022

been well recognized as described above, little is known about the interactions of engineered DNA with natural organic matter (NOM) in typical aquatic environments. Natural organic matter, including humic substances, proteins, polysaccharides, etc., is ubiquitous in the environment (Philippe and Schaumann, 2014), and their interactions with engineered DNA interfere the performance of DNA-based applications. For aptasensors, a positive correlation between NOM concentration (0–3.6 mg C/L) and the extent of performance degradation has been observed (Vogiazi et al., 2021), however, higher NOM concentrations (from 4 to 16 mg C/L) were also reported to exert no significant influence on the performance (Akki et al., 2015; Park et al., 2022). Among various types of aptasensor, colorimetric aptasensors typically involve the use of DNA-coated gold nanoparticles (Au NPs). The Au NPs are stabilized by the DNA coating in the presence of high-concentration salts, and the introduction of the target triggers preferential binding of DNA aptamer and causes the aggregation of Au NPs. Such systems are dependent on salt-induced aggregation and susceptible to interference from matrices (e.g., NOM or other constituents) (Akki and Werth, 2018). For example, low recovery of target was observed when the target was doped in milk samples (Yan et al., 2017). Other than aptasensors, NOM can also impact the functionality of DNA tracers. Adsorption of DNA tracers to NOM can lead to low recovery and unprecise detection (Liao et al., 2018; Pang et al., 2020). These reports highlight the need to elucidate the interaction(s) between engineered DNA and NOM, and also the associated change of nanoparticle aggregation behaviors, which will benefit the development of DNA-based applications in more realistic scenarios.

Previous studies investigating the interactions between DNA and NOM have been mostly conducted with (natural) dsDNA with a long chain (thousands of base pairs) (Lu et al., 2012; Nguyen and Chen, 2007; Nguyen and Elimelech, 2007; Qin et al., 2018). For example, divalent cations formed bridges between the phosphate groups of DNA and the carboxyl groups of NOM, while monovalent cations only screened the negative charges (Nguyen and Chen, 2007; Nguyen and Elimelech, 2007). However, variations in DNA properties (e.g., double-stranded or single-stranded, length, and sequence) may increase the complexity of their interactions with NOM. Smaller DNA fragments (2.69 kbp) were reported to have preferential adsorption to soil compared to larger fragments (11.19 and 23 kbp) due to their faster diffusion rates and/or the size exclusion of available binding sites (Ogram et al., 1994). The phosphate groups of dsDNA were deemed as the major interaction sites with NOM (Lu et al., 2012; Nguyen and Chen, 2007; Nguyen and Elimelech, 2007) while the exposed nucleobases of ssDNA also participated in the interaction with graphene oxide (He et al., 2010; Liu et al., 2020). The preferential interaction of cations with guanine bases in the ssDNA affected the ion distribution along the DNA strands, resulting in varied DNA layer thickness and drastically different colloidal stability of the coated particles (Peng et al., 2022). Little attention has been paid to (engineered) short-chain ssDNA (e.g., $<$ 100 nucleobases, the typical length of a DNA aptamer (Zhou et al., 2010)), which behaves distinctively from natural dsDNA in aquatic systems. As such, there is a critical knowledge gap in understanding the interactions of short-chain ssDNA with NOM, which expectedly have profound implications for the rational design of engineered DNA for aquatic applications, such as DNA-based sensor/adsorbent and DNA tracer, among other emerging applications.

In this study, we investigated the interaction(s) between ssDNA and NOM by examining the impact of NOM on the colloidal stability of ssDNA-coated nanoparticles. Molecular level interaction mechanisms were revealed by characterizing the resulting products using a suite of microscopic and spectroscopic techniques (FTIR, Raman, Fluorescence, and TEM). Following our earlier work (Peng et al., 2022), ssDNA-coated gold nanoparticles (DNA-Au NPs) with four different ssDNA coatings (systematically varied in length and sequence) were studied. Two humic acids (Suwannee River humic acid (SRHA), an aquatic humic substance, and Aldrich humic acid (AHA), a terrestrial humic substance (Hur and Schlautman, 2003)), along with two humic-like NOM from local water matrices in Hong Kong (river water and wastewater effluent) were studied as the representative NOM. Our study revealed the dependence of ssDNA-NOM interaction on the aromaticity of NOM and the cation bridging effect (especially Ca^{2+}). A strong interaction could result in a complete shielding of the ssDNA by NOM, potentially sabotaging the functionality of ssDNA (e.g., the specific binding of aptamer to target and the hybridization of DNA barcode). Our findings provide new insights into the functioning of engineered ssDNA in complex aquatic matrices and directions to optimize the general design of DNA-based system for various aquatic applications (e.g., selection of DNA tracer and DNA aptamer and proper pretreatment strategy).

2. Experimental

2.1. Materials

Citrate-capped 20 nm spherical Au nanoparticles (Ted Pella, Inc.) were used for the synthesis of DNA-Au NPs. Four single-stranded DNA (ssDNA) with carefully designed sequences and 3' end thiol modification were purchased from IDT (Integrated DNA Technologies, Inc.; denoted as DNA_{15}, DNA_{25}, DNA_{25C}, and DNA_{40}, Fig. 1). The design of DNA_{15}, DNA_{25}, and DNA_{40} aimed at investigating the effect of DNA length, while the design of DNA_{25} and DNA_{25C} was to evaluate the effect of DNA sequence (Peng et al., 2022). Suwannee River humic acid (SRHA) was purchased from International Humic Substances Society (IHSS, standard III), and Aldrich humic acid (AHA) was purchased from Sigma-Aldrich.

2.2. Synthesis of DNA-Au NPs

DNA-Au NPs were synthesized using the salt-aging method (Liu and Liu, 2017; Mirkin et al., 1996), and the detailed procedure has been provided previously (Peng et al., 2022). Briefly, the ssDNA and Au NP suspension were incubated with stepwise addition of NaCl solution (2 M) to increase the salt concentration to 0.1 M. Excess reagents were removed by centrifugation three times. The DNA-Au NPs were redispersed in deionized water and stored at 4 °C until use.

2.3. Preparation of NOM solutions

SRHA and AHA stock solutions were prepared by dissolving humic substances in MilliQ water under pH 10.5 and subsequently filtering the mixture using a 0.45 μm membrane filter. The chemical characteristics of SRHA and AHA were assessed by UV/vis spectroscopy (Biochrom Libra S35), fluorescence spectroscopy (FLS920, Edinburgh Instruments), Raman spectroscopy (i-Raman Plus, B&W TEK), and FTIR (Spectrum

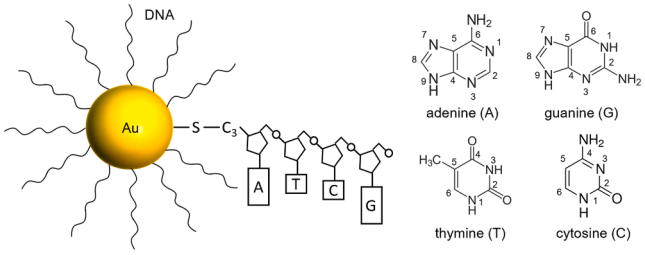

DNA Sequences (3' to 5')	
DNA_{15}	HS-$(CH_2)_3$-AAAAAAAAAA GACTC
DNA_{25}	HS-$(CH_2)_3$-AAAAAAAAAA GACTCATACTCACCT
DNA_{25C}	HS-$(CH_2)_3$-AAAAAAAAAA CTGAGTATGAGTGGA
DNA_{40}	HS-$(CH_2)_3$-AAAAAAAAAA GACTCATACTCACCT GACTCATACTCACCT

Fig. 1. Schematic of a DNA-coated gold nanoparticle (DNA-Au NP) and the molecular structure of the four nitrogenous bases. The schematics are not drawn to scale and for illustrative purposes only. Sequences of the four DNA strands used in this study are listed in the table.

Two PerkinElmer) (Details in Text S1). Specific UV absorbance at 254 nm ($SUVA_{254}$) was calculated as the UV absorbance at 254 nm divided by the total organic carbon (TOC; mg C/L, determined by TOC-L, Shimadzu) and 1 cm quartz cell path length. Bulk elemental compositions and functional group compositions of SRHA and AHA retrieved from previous works are summarized in Table S1.

2.4. Aggregation kinetics of DNA-Au NPs in the presence of NOM and electrolytes

Aggregation kinetics of DNA-Au NPs (10 mg Au/L) in the presence of NOM (SRHA or AHA, 2.7 mg C/L) were analyzed in three electrolytes (NaCl: 0.1–4 M; $CaCl_2$: 0–100 mM; $MgCl_2$: 0–100 mM) by time-resolved dynamic light scattering (TR-DLS; Zetasizer Nano ZS90, Malvern Instruments) following our previous work (Peng et al., 2022). The pH was unadjusted and determined to be 6.4 ± 0.2. Stock solution of SRHA or AHA was mixed with DNA-Au NPs, followed by the addition of salts. Attachment efficiency (α) was determined to be the ratio of the initial rate of change in the reaction-limited regime over that in the diffusion-limited regime. Critical coagulation concentration (CCC), served as an indicator for colloidal stability, was obtained from the intersection of extrapolated lines of reaction-limited and diffusion-limited regimes.

2.5. Stability of DNA-Au NPs in complex aquatic matrices

River water was collected from the Lam Tsuen River located in Tai Po, Hong Kong. Wastewater effluent was obtained from the secondary effluent of Tai Po Wastewater Treatment Plant in Hong Kong. The water samples were filtered by 0.45 μm filters and analyzed with regard to pH, TOC, conductivity, and cation concentration (Dionex Integrion HPIC System, Thermo Scientific). The organic matter in river water and wastewater (denoted as ROM and WOM, respectively) were characterized by fluorescence and Raman spectroscopies.

Initial aggregation kinetics (30 min) of DNA-Au NPs in river water or wastewater effluent were measured at a particle concentration of 5 mg Au/L with or without dosed SRHA/AHA (10 mg C/L). Particle size was monitored via TR-DLS at 30 s interval for 30 min. For long-term stability (21 days) of DNA-Au NPs, initial dosing of DNA-Au NPs was 500 μg Au/L and the concentration of suspended DNA-Au NPs was determined by inductively coupled plasma optical emission spectroscopy (ICP-OES, Agilent 720). The dosing of SRHA/AHA was 1 mg C/L or 5 mg C/L.

2.6. Characterization of DNA-NOM interactions

The hydrodynamic diameter and electrophoretic mobility (EPM) of SRHA/AHA-adsorbed DNA-Au NPs were determined using Zetasizer Nano ZS90. The structures of DNA-Au NP aggregates with SRHA/AHA present in three electrolytes (NaCl, $MgCl_2$, and $CaCl_2$) were examined by transmission electron microscopy (TEM, JEOL JEM-2010) and scanning transmission electron microscopy (STEM, Talos™ F200X G2) equipped with high angle annular dark field (HAADF) detector and energy-dispersive X-ray spectroscopy (EDS) detector. The Raman and FTIR spectra of NOM-adsorbed DNA-Au NPs were recorded. Detailed procedures are provided in Text S1.

2.7. Urea/SDS induced desorption of NOM from DNA-Au NPs

NOM (5 mg C/L) was incubated with DNA_{25}-Au NPs (5 mg Au/L) in 50 mM NaCl overnight to allow adsorption to reach equilibrium (pH 6.3 ± 0.2). After centrifugation (11000 rpm, 20 min) and removal of the supernatant, the NOM-adsorbed DNA-Au NPs were dispersed in solutions containing different solutes (50 mM NaCl; 50 mM NaCl, and 1 or 6 M urea; 50 mM NaCl, and 1% or 10% sodium dodecyl sulfate (SDS)). After 45 min, the released NOM was quantified by fluorescence spectroscopy.

3. Results and discussion

3.1. Characterization of DNA-Au NPs and NOM

DNA strands were thiol-modified at their 3' end and attached to the particle surface via Au-S covalent bonds, forming a densely-packed DNA layer (Mirkin et al., 1996) (Fig. 1). Four DNA strands with systematically varied sequences and lengths were used to synthesize DNA-Au NPs, denoted as DNA_{15}-Au, DNA_{25}-Au, DNA_{25C}-Au, and DNA_{40}-Au, respectively. Such design aimed at singling out the effect of DNA length (i.e., DNA_{15}, DNA_{25}, and DNA_{40}) and the effect of DNA sequence (i.e., DNA_{25} and DNA_{25C}) on their interactions with NOM. Detailed characterization of these particles has been reported in our earlier work (Peng et al., 2022). The hydrodynamic sizes of the four DNA-Au NPs were 35.4 ± 1.5 nm of DNA_{40}-Au, 33.1 ± 0.5 nm of DNA_{25C}-Au, 31.2 ± 1.7 nm of DNA_{25}-Au, and 30.8 ± 1.5 nm DNA_{15}-Au, respectively.

Fig. 2a presents the UV/vis spectra of SRHA and AHA (2.7 mg C/L in water). AHA had higher absorbance than SRHA in both the UV and visible light wavelength ranges. Absorbance at 254 nm is characteristic of aromatic regions (Korshin et al., 2009), whereas absorbance at 280 nm is positively correlated to molecular weight (Chin et al., 1994). The observed higher absorbance of AHA at 280 nm was consistent with the reported more high-molecular-weight portion (> 100 kDa) in AHA than SRHA (*ca.* 20% for AHA vs 5% for SRHA) (Kim et al., 2006). Due to different humification environments, SRHA is typically comprised of relatively small and polar moieties, while AHA has more nonpolar and aromatic contents (Grasso et al., 1990; Hong and Elimelech, 1997). The $SUVA_{254}$ of SRHA and AHA were calculated to be 6.2 ± 0.1 and 9.0 ± 0.1, respectively, suggesting a higher aromatic content of AHA (Abbt-Braun et al., 2004) and being in agreement with our previously reported values (Jiang et al., 2017).

The EEMs of SRHA and AHA showed a similar excitation maximum at around 330 nm, and SRHA showed an obvious emission peak at around 460 nm while AHA had a broad emission peak from 450 to 550 nm (Fig. 2c-d). The excitation/emission wavelengths are representative of humic-like peak C fluorophore (Coble, 1996). Emission scan at 330 nm excitation confirmed the emission peak of AHA at around 520 nm (Fig. 2b). A blue-shifted emission maximum of SRHA indicates a decrease in the π-electron system, such as a lower number of aromatic rings (Coble, 1996), consistent with the lower aromaticity as suggested by the smaller $SUVA_{254}$ value of SRHA. Also, it has been suggested that long emission wavelengths (> 500 nm) could be attributed to the presence of greatly conjugated systems, such as linearly condensed aromatic rings and other unsaturated bond systems (Rodríguez et al., 2014; Sierra et al., 2005), in accordance with the higher aromaticity of AHA as suggested by a larger $SUVA_{254}$ value.

3.2. Aggregation kinetics of DNA-Au NPs in the presence of NOM

The aggregation kinetics of DNA-Au NPs in the presence of SRHA or AHA were investigated in NaCl, $MgCl_2$, and $CaCl_2$ electrolytes, respectively. Distinct reaction-limited and diffusion-limited regimes of DNA-Au NPs were observed (Fig. S1). The CCC values were determined as the intersections of the extrapolated lines of these two regimes and compared in Fig. 3. The CCC values of DNA-Au NPs without NOM were retrieved from our previous work (Peng et al., 2022).

The presence of SRHA increased the CCC values of DNA_{15}-Au from 451 mM to 489 mM NaCl, from 2.2 mM to 3 mM $MgCl_2$, and from 2.2 mM to 2.7 mM $CaCl_2$, respectively (Fig. 3). Similar enhanced colloidal stability was observed for the other three DNA-Au NPs, regardless of the DNA sequence and length. The enhancement of colloidal stability by the presence of NOM has been extensively reported (Jiang et al., 2017; Loosli et al., 2013; Nason et al., 2012), and such effect was attributed to the enhanced (electro)steric repulsion imparted by adsorbed NOM (Chen and Elimelech, 2007). The EPMs of SRHA-adsorbed DNA-Au NPs were either less negative (in NaCl electrolyte) or similar (in $MgCl_2$ or

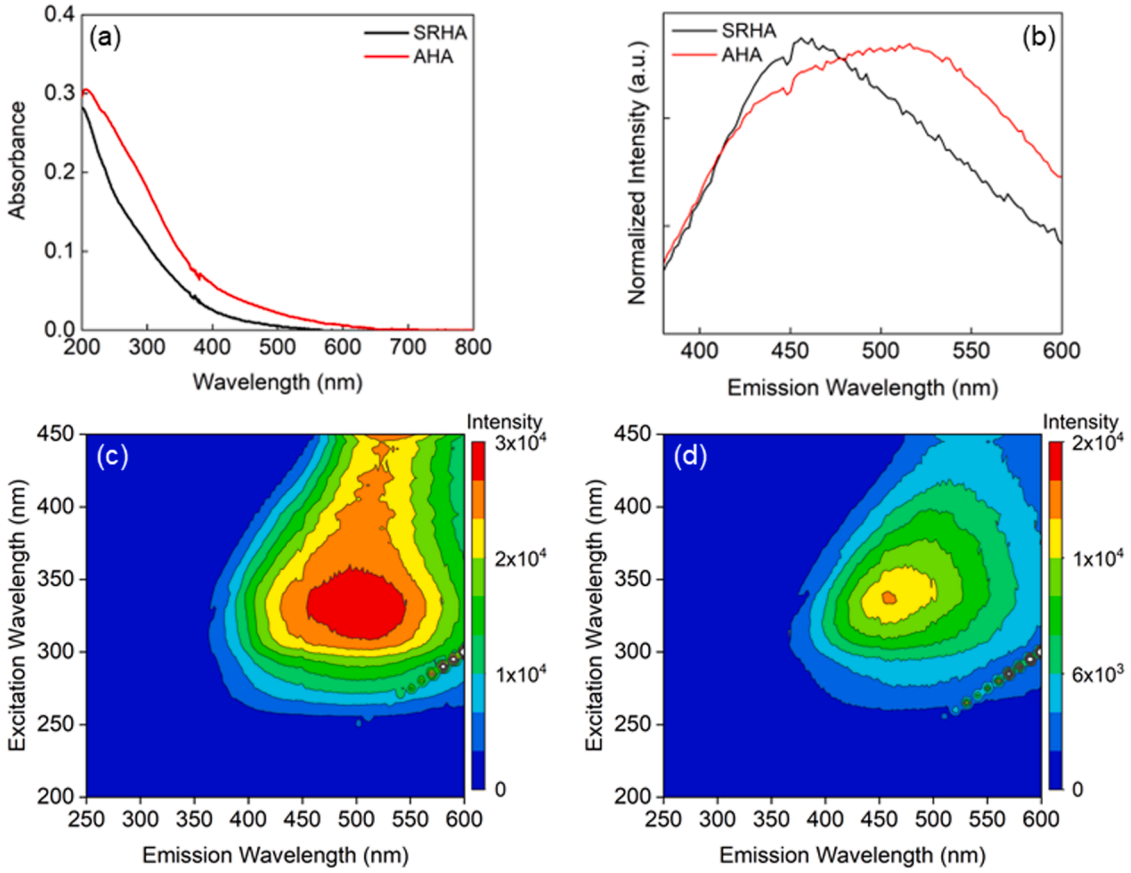

Fig. 2. Spectroscopic characterization of SRHA and AHA; (a) UV/vis spectra (2.7 mg C/L); (b) normalized emission scan spectra at excitation wavelength of 330 nm; (c) and (d) excitation emission matrix (EEM) of SRHA and AHA, respectively.

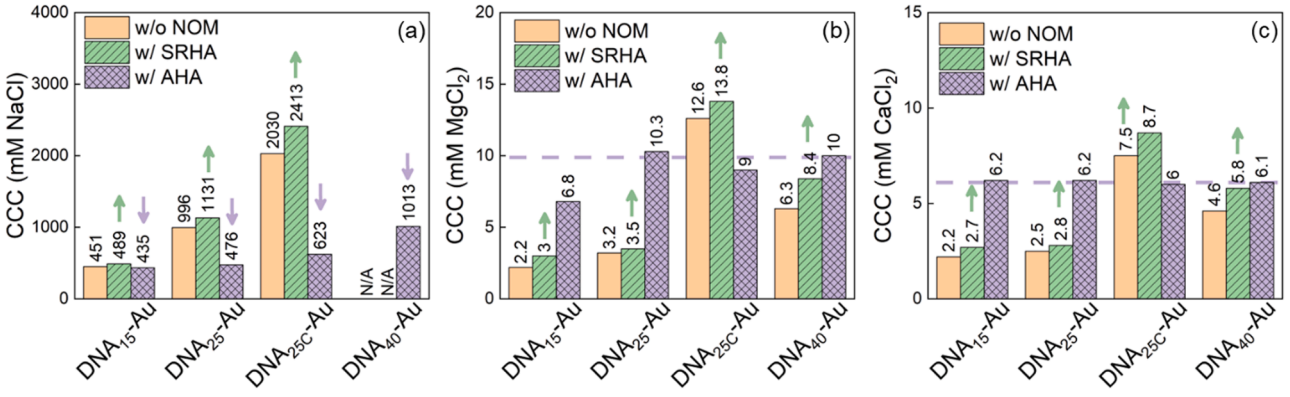

Fig. 3. Critical coagulation concentration (CCC) of DNA-Au NPs (10 mg Au/L) with or without the presence of NOM (2.7 mg C/L) in (a) NaCl; (b) $MgCl_2$; (c) $CaCl_2$. The CCC values of DNA-Au NPs without NOM were retrieved from our previous work (Peng et al., 2022). The NaCl CCC values of DNA_{40}-Au without NOM or with SRHA were not obtained due to a lack of observed diffusion-limited aggregation in the NaCl concentrations tested. Upward/downward arrows (green/purple) indicate increased/decreased CCC values with the presence of NOM compared to those without NOM. Dash lines (purple) indicate the similar CCC values with the presence of AHA.

$CaCl_2$ electrolyte) to the 'bare' DNA-Au NPs (Text S2 and Fig. S3), indicating that the enhanced colloidal stability mainly arose from stronger steric repulsion. The order of stability among the four DNA-Au NPs with the presence of SRHA was the same as that without SRHA (Peng et al., 2022), i.e., (1) in NaCl electrolyte: DNA_{40}-Au > DNA_{25C}-Au > DNA_{25}-Au > DNA_{15}-Au and (2) in $MgCl_2$ and $CaCl_2$ electrolytes: DNA_{25C}-Au > DNA_{40}-Au > DNA_{25}-Au > DNA_{15}-Au.

Unlike SRHA, the presence of AHA significantly changed the stability of DNA-Au NPs, and the effect showed a strong dependency on the co-existing cations. In NaCl electrolyte, the presence of AHA lowered the CCC values of all four DNA-Au NPs (Fig. 3a). For example, the CCC value of DNA_{25C}-Au decreased significantly from 2030 mM to 623 mM NaCl. Although the colloidal stability of DNA-Au NPs was reduced by the presence of AHA, the order of stability did not change compared to that without AHA present, i.e., DNA_{40}-Au > DNA_{25C}-Au > DNA_{25}-Au > DNA_{15}-Au. In divalent electrolytes ($MgCl_2$ and $CaCl_2$), interestingly, the presence of AHA brought the stability of DNA-Au NPs to a similar level (i.e., similar CCCs, Fig. 3b-c) regardless of the original ssDNA coatings,

which was completely different from the effect of SRHA. The CCC values of DNA-Au NPs with AHA present were *ca.* 6 mM $CaCl_2$ and *ca.* 10 mM $MgCl_2$ (with the exception of DNA_{15}-Au in $MgCl_2$ electrolyte, 6.8 mM). In either electrolyte, the similar EPMs of DNA-Au NPs with or without the presence of AHA (Fig. S3) indicated that mechanism(s) other than electrostatic interactions should be accounted for inducing such change in colloidal stability.

3.3. Mechanisms underlying the distinct effects of NOM on particle stability

3.3.1. Adsorption of NOM onto DNA-Au NPs

The interaction between DNA-Au NPs and NOM (SRHA/AHA) was first probed by fluorescence spectroscopy (Text S3 and Fig. S4-6). Due to fluorescence quenching of Au NPs (Liu and Liu, 2017), the fluorescence intensity of NOM was lowered after adsorption (Figs. S4a and e, S5a and e, and S6). Stronger quenching of the AHA fluorescence by DNA-Au NPs was observed compared to SRHA (Fig. S6), suggesting a stronger interaction (i.e., adsorption) between AHA and the ssDNA coating. For example, by calculating the intensity change at emission maximum (460 nm for SRHA and 520 nm for AHA, excitation wavelength = 330 nm), the peak intensity of SRHA was reduced by 8%, while that of AHA was reduced by 24%. When additional salts ($NaCl/MgCl_2/CaCl_2$) were introduced, the fluorescence intensity of AHA was further decreased while the emission peak intensity of SRHA barely changed (Text S3 and Fig. S4-6). Both NOM and DNA-Au NPs were negatively charged, therefore the adsorption of NOM should be attributed to interactions other than electrostatic attraction, such as hydrogen bonding, hydrophobic interactions, π-π interactions, cation bridging, etc. (Philippe and Schaumann, 2014).

To understand the NOM-DNA interaction mechanism(s), we first examined the FTIR spectra of NOM-adsorbed DNA-Au NPs in $CaCl_2$/NaCl electrolytes, respectively. The adsorption of NOM in $CaCl_2$ electrolyte induced a spectral change at *ca.* 1580 cm^{-1} (Fig. 4a and c), and the extent of which is more pronounced in the spectra of AHA-adsorbed ones and proportional to the adsorbed amount (AHA:Au = 1:1). The results suggested that the ssDNA coating interacted more strongly with AHA than SRHA, consistent with the aforementioned fluorescence study. Due to the strong overlap of absorption in the IR spectra of the four nucleobases (Alex and Dupuis, 1989; Tsuboi, 1970), correlating the interaction between SRHA/AHA and a specific nucleobase was difficult. Nevertheless, an attenuation of the peak at 1466 cm^{-1} after NOM adsorption, which symbolizes the in-plane vibrations of the nucleobases (e.g., NH and CH in the ring structures (Tsuboi, 1970); molecular structures shown in Fig. 1), was observed in both electrolytes ($CaCl_2$ and NaCl; Fig. 4a, c, and e), implying that the ssDNA-NOM interactions could have occurred through π-π interactions. Furthermore, we observed attenuated peaks at 1730 cm^{-1} (C═O stretching of nucleobases (guanine, thymine, and cytosine, Fig. 1)), 1277 cm^{-1} (asymmetric stretching of phosphate), and 1073 cm^{-1} (symmetric stretching of phosphate) (Alex and Dupuis, 1989; Tsuboi, 1970), which may stem from the binding of cations and/or hydrogen bonding (Park et al., 2013) between NOM and the ssDNA coating. These interaction sites (i.e., C═O of nucleobases and phosphate groups) indicated by the FTIR results were consistent with our previous work (Peng et al., 2022), in which we used molecular dynamics simulations to investigate the interaction between Ca^{2+} and DNA strands. To further probe the interactions, we used urea and SDS to induce possible desorption of NOM from DNA-Au NPs in NaCl electrolyte (excluding cation bridging). Urea breaks hydrogen bonds (Liu et al., 2020) and SDS breaks both hydrogen bonds and hydrophobic interactions (Schmid et al., 2017), while π-π interactions are not disturbed. As shown in Fig. 4g, urea induced the desorption of AHA from DNA-Au NPs, and the effect of which was more pronounced at higher urea concentration (6 M, *ca.* 10% AHA desorbed). SDS also induced the desorption of AHA (*ca.* 14% AHA desorbed with 10% SDS). These results suggest that hydrogen bonding and/or hydrophobic interactions contributed to the adsorption of AHA onto DNA-Au NPs, however, a quantitative distribution of each AHA adsorption mechanism cannot be achieved. Overall, less than 15% of AHA were desorbed even at 6 M urea or 10% SDS condition, suggesting that π-π interaction was the major mechanism responsible for AHA adsorption. On the other hand, desorption of SRHA induced by urea or SDS was not observed (Fig. 4h), indicating that π-π interaction was likely the only mechanism responsible for SRHA adsorption. Therefore, the exposed nucleobases of ssDNA played a significant role in its interaction with NOM via π-π interactions. The stronger adsorption of AHA than SRHA onto DNA-Au NPs was due to its higher aromaticity (indicated by the aromatic carbon content (Table S1) and $SUVA_{254}$) and capability to form hydrogen bonding/hydrophobic interactions with the ssDNA coating.

Raman spectra revealed more details of the interaction between NOM and the ssDNA. The adsorption of AHA in $CaCl_2$ electrolyte completely shielded the characteristic peaks of adenine (734 cm^{-1}) and nucleobases (1250–1500 cm^{-1}) (Alex and Dupuis, 1989; Otto et al., 1986) (Fig. 4b). The spectra of AHA-adsorbed DNA-Au NPs became the same as that of pure AHA even at a low carbon-to-gold ratio (AHA:Au = 1:10). On the other hand, the characteristic peaks of adenine and nucleobases after SRHA adsorption remained in the spectra, albeit attenuated (Fig. 4d). With more SRHA adsorbed (SRHA:Au increased from 1:10 to 1:1), the peak of adenine became weaker and the peaks from SRHA (e.g., 1190 and 1517 cm^{-1}) became apparent. Similar pattern was observed for the NOM-adsorbed DNA_{25C}-Au NPs in $CaCl_2$ electrolyte as well (Fig. S7), likely due to that the minor differences in DNA_{25} and DNA_{25C} did not significantly impact their interactions with NOM. In NaCl electrolyte, neither SRHA nor AHA was able to completely shield the original ssDNA coating, as suggested by the remaining peaks of adenine and nucleobases after adsorption (Fig. 4f). The relatively weaker peaks of adenine and nucleobases in the spectrum of AHA-adsorbed DNA_{25}-Au compared to the SRHA-adsorbed one was in line with the stronger interaction between AHA and the ssDNA coating. The lack of complete shielding by adsorbed AHA in NaCl electrolyte suggested that divalent cation bridging between the phosphate groups of DNA and the carboxyl groups of NOM (Lu et al., 2012; Nguyen and Chen, 2007) also played a significant role in the adsorption process of AHA in $CaCl_2$ electrolyte.

3.3.2. Intermolecular Interactions of NOM

Aggregation of Au NPs shortens their interparticle distance and causes the suspension color to change from red to purple (Storhoff et al., 2000). Such color change was observed for the aggregated DNA-Au NPs without NOM present or with SRHA present in all three electrolytes (Fig. 5c inset and S8b-c). However, the colors of aggregated DNA-Au NPs with AHA present were reddish-purple (Fig. 5a inset) and showed a dependency on the presence of cations (Fig. S8d-e). From Na^+, Mg^{2+}, to Ca^{2+}, the color of the suspensions gradually transitioned from purple to magenta, suggesting increased interparticle distance of the aggregated Au NPs. More details regarding the colors of aggregated DNA-Au NPs are given in Text S4.

To elucidate the underlying mechanism(s) causing the discrepancy in color change, we examined the structure of aggregated DNA_{25}-Au with NOM present via TEM and EDS elemental mapping. In the presence of both Ca^{2+} and AHA, we observed light shadowy areas bridging DNA-Au NPs (Fig. 5a and S9a-c). Such bridging areas were also observed in the HAADF images (Fig. 5b). The corresponding EDS elemental mapping showed that the elemental distribution of P (from DNA backbone) and S (from thiol group in DNA, Fig. 1) matched well with that of Au, suggesting that the DNA strands were on Au NPs. The elemental distribution of N and O highly overlapped with the bridging areas (Fig. 5b insets), especially the O distribution, indicating the areas were indeed AHA molecules. The intermolecular bridging of AHA molecules (both adsorbed and unadsorbed) likely occurred via calcium complexation (Chen and Elimelech, 2007; Liu et al., 2011; Schwyzer et al., 2013). On the contrary, the intermolecular bridging of SRHA molecules was hardly

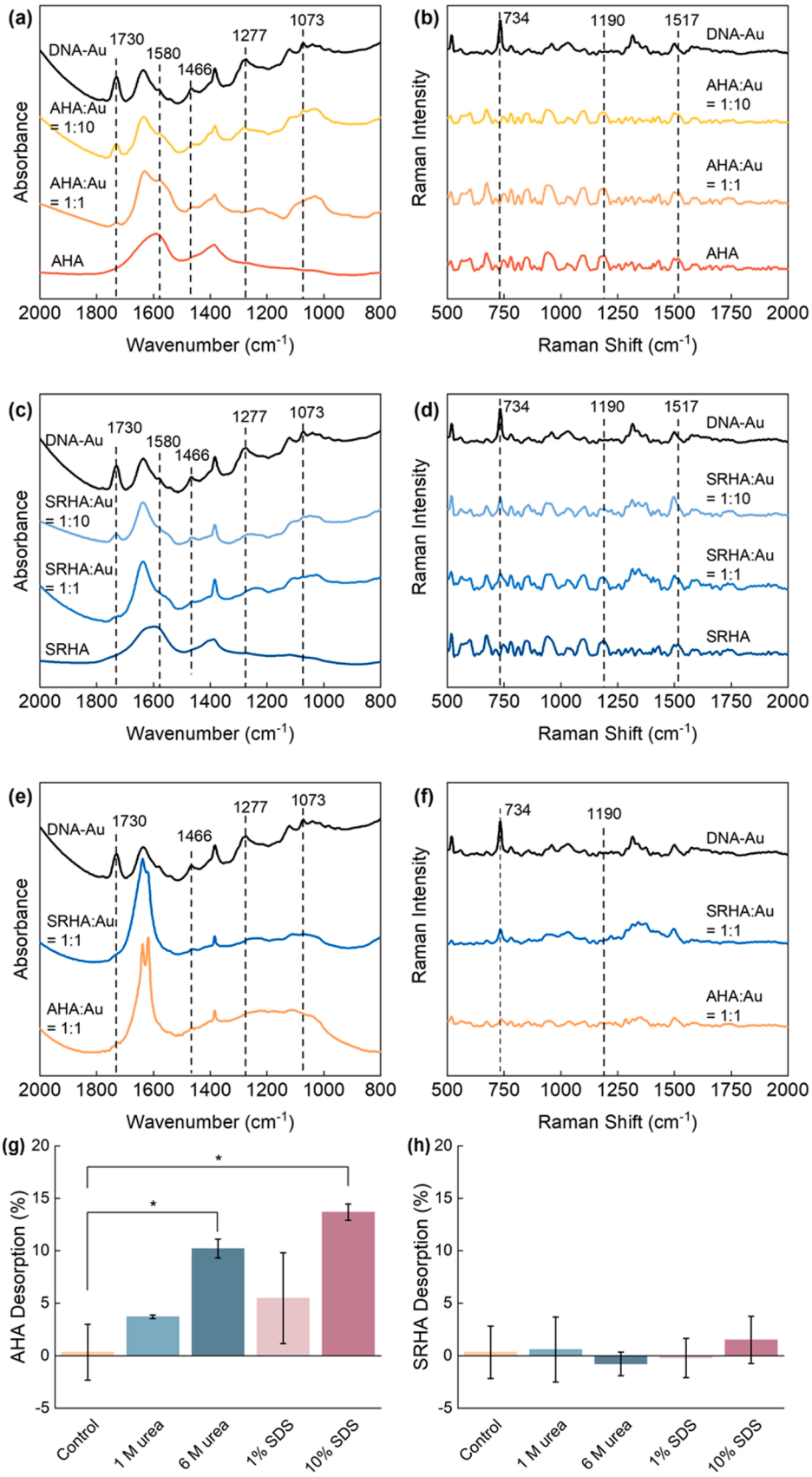

Fig. 4. (a-f) FTIR and Raman spectra of SRHA/AHA adsorbed DNA_{25}-Au in (a-d) 0.5 mM $CaCl_2$ or (e-f) 50 mM NaCl. SRHA/AHA:Au refers to the carbon-to-gold ratio during sample preparation (see details in Text S1). (g-h) Urea or SDS induced desorption of (g) AHA or (h) SRHA from NOM-adsorbed DNA_{25}-Au NPs. Error bars indicate one standard deviation of at least three replicates. Asterisks indicate significant difference (one-way ANOVA test followed by the Tukey test for multiple comparisons, $p < 0.05$).

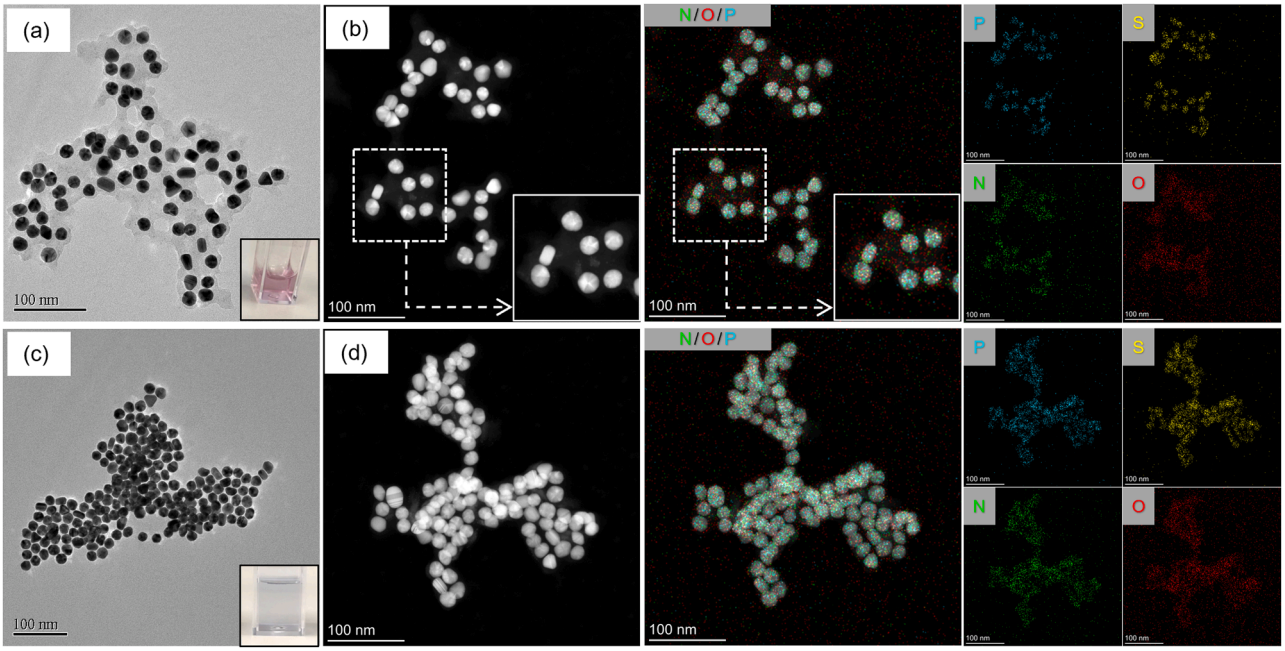

Fig. 5. Morphology and microscopic structure of aggregated DNA_{25}-Au NPs (10 mg/L) in the presence of 10 mM Ca^{2+} and 2.7 mg C/L NOM. (a-b) aggregated particles with AHA present examined by (a) TEM and (b) HAADF-STEM and the corresponding EDS elemental mapping; insets show the enlarged selected area (white dashed box). (c-d) aggregated particles with SRHA present examined by (c) TEM and (d) HAADF-STEM and the corresponding EDS elemental mapping.

observed (Figs. 5c-d and S10a-c), and the aggregate structure was similar to the aggregated DNA-Au NPs without NOM present (Fig. S11). The interparticle distance observed with AHA present was apparently larger than the other two scenarios (with SRHA or without NOM), in agreement with the magenta color of the aggregate suspension (Fig. 5a inset). The aggregated particles with SRHA present or without NOM were closely packed, in line with the purple colors of their aggregate suspensions (Fig. 5c inset).

Similar bridging of the AHA molecules by Mg^{2+} was observed (Fig. S9d-f), but to a less extent and only occurred at high concentrations (e.g., 20 mM Mg^{2+}) (Text S5 and Fig. S12-13), in agreement with the intermediate reddish-purple color of aggregate suspension (Fig. S8e). Such discrepancy in the effect of Mg^{2+} and Ca^{2+} stemmed from the weaker electronegativity and larger hydrated radius of Mg^{2+} (Stankus et al., 2011). Interestingly, although the bridging effect was not expected in NaCl electrolyte because Na^{+} only screens the negative charges, similar light shadowy areas linking aggregated particles was observed with the presence of AHA (Fig. S9g-l), but not with SRHA (Fig. S10d-f). Such intermolecular interactions of AHA molecules are speculated to occur through π-π interaction due to their high aromaticity (Ghosh et al., 2008; Nason et al., 2012).

The bridging of NOM molecules by divalent cations has been widely reported (Chen and Elimelech, 2007; Ghosh et al., 2008; Huynh and Chen, 2011; Liu et al., 2011; Nason et al., 2012; Stankus et al., 2011), and the carboxyl groups have been recognized as the binding sites for cations. Although the carboxyl group density was found to be positively related to the bridging effectiveness (Lu et al., 2012), it does not seem to be the only parameter determining the bridging effect. For example, the bridging of SRHA (standard II), which has 15% carboxyl carbon (Table S1), has been reported (Chen and Elimelech, 2007; Huynh and Chen, 2011; Liu et al., 2011), but the bridging of SRHA (standard I) with a higher carboxyl content (19% carboxyl carbon, Table S1) was not observed (Huangfu et al., 2013). Other parameters, such as the position of carboxyl groups in the polymer chain (Labille et al., 2005), might also need to be taken into consideration. In our study, the bridging mediated by divalent cations was only observed with AHA but not SRHA, which was consistent with the aggregation profile of pure SRHA/AHA in the electrolytes (Fig. S2). Only in $CaCl_2$ electrolyte of a high concentration (50 mM), the SRHA molecules formed clusters that can be steadily detected by the DLS instrument (Fig. S2d), while the aggregation of AHA molecules was observed in both $CaCl_2$ and $MgCl_2$ electrolytes (Fig. S2b-c). The higher carboxyl content of AHA than SRHA (standard III used in this study) (Table S1) may partially contribute to the observed phenomenon. More efforts are required to reveal the underlying mechanism of such divalent cation bridging in future.

3.3.3. *Proposed interaction mechanisms*

The adsorption of NOM to ssDNA and subsequent impact on the colloidal stability of DNA-Au NPs in simple electrolytes showed a dependency on both the properties of NOM and cations (Fig. 6). In divalent electrolytes ($MgCl_2$ and $CaCl_2$), the adsorbed AHA molecules completely shielded the original ssDNA coating, which was facilitated mainly by both π-π interaction and divalent cation bridging. The AHA coating determined the stability of the coated nanoparticles, which explained the similar CCC values of the four AHA-adsorbed DNA-Au NPs in divalent electrolytes (Fig. 3b-c). On the contrary, the adsorption of AHA in NaCl electrolyte did not completely shield the original ssDNA coating. As such, the original ssDNA coating still played a role in the colloidal stability, explaining the same order of stability as the 'bare' DNA-Au NPs (Fig. 3a). The order of stability for the four 'bare' DNA-Au NPs was determined by ssDNA coating thickness, which was influenced by the coating properties (DNA strand length, sequence, and loading) and cations (preferential interaction with guanine base), as discussed in our previous work (Peng et al., 2022). The intermolecular attractions from the adsorbed AHA molecules led to the reduced colloidal stability (lower CCC values).

The adsorption of SRHA onto DNA-Au NPs was limited, largely due to the relatively weak π-π interactions between SRHA and ssDNA. Furthermore, the stabilization of DNA-Au NPs by adsorbed SRHA was only observed in high SRHA concentration (100 mg C/L) in $CaCl_2$ electrolyte but not in $MgCl_2$ electrolyte (Text S5 and Fig. S12), suggesting that Ca^{2+} bridged the ssDNA with SRHA while Mg^{2+} did not, and the bridging effect was relatively weaker compared to that with AHA. As a result, the adsorption of SRHA did not completely shield the original ssDNA coating in all three electrolytes. The original ssDNA coating determined the particle stability, explaining the same order of colloidal

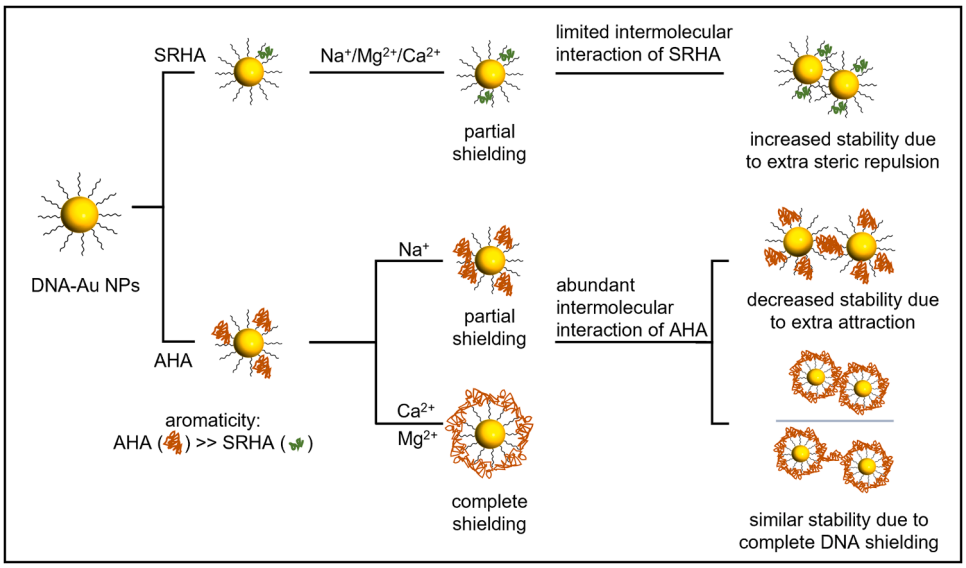

Fig. 6. Schematic illustration of the interactions between SRHA/AHA and DNA-Au NPs, and the subsequent impact on the colloidal stability of DNA-Au NPs. The schematics are not drawn to scale and for illustrative purposes only.

stability of the four SRHA-adsorbed DNA-Au NPs as the 'bare' DNA-Au NPs (Fig. 3). The limited intermolecular interaction of SRHA molecules and the extra steric repulsion provided by the adsorbed SRHA molecules collectively contributed to the minor increase of CCC values.

3.4. Interaction of ssDNA with NOM in real water samples

3.4.1. Interaction with the real water organic matter

The wastewater effluent and river water characteristics are summarized in Table S2. The high ionic strength of the wastewater effluent (conductivity = 13360 μS/cm, saline wastewater, a unique feature in Hong Kong due to seawater toilet flushing), especially high concentration of divalent cations (10 mM Mg^{2+} and 2.9 mM Ca^{2+}), induced the rapid aggregation of both DNA_{25}-Au and DNA_{25C}-Au in the 30-min kinetics study (Fig. 7a-b; more details in Text S6). A slower aggregation of DNA_{25C}-Au was observed due to the guanine-rich sequence of DNA_{25C} (Peng et al., 2022). On the contrary, the stability of DNA_{25}-Au and DNA_{25C}-Au did not differ in the 21-day study (Fig. 7c and S14a), with approximately 20% of the particles remained suspended after 21 days. This discrepancy in the 30-min/21-day studies was due to the varied overcoating of wastewater organic matter (WOM, TOC = 7.0 mg C/L) onto the DNA-Au NPs. The fluorescence analysis of WOM revealed their humic-like nature (a maximum fluorescence of peak C, Fig. S15a) and slightly lower aromaticity than SRHA (Fig. S15c) (Coble, 1996; Rodríguez et al., 2014). Different dosing of DNA-Au NPs in the 30-min (5 mg Au/L) and the 21-day (0.5 mg Au/L) studies resulted in different carbon-to-gold or carbon-to-DNA (mass) ratios (WOM:Au = 1.4 and 14, respectively; WOM:DNA = 140 and 1400, respectively), which impacted the amount of adsorbed WOM. The Raman spectra of WOM-adsorbed DNA-Au NPs confirmed that more WOM were adsorbed at higher WOM:Au ratio (Fig. 7e). The peak of adenine (734 cm^{-1}) disappeared and WOM peaks became apparent (e.g., 942 and 1003 cm^{-1}) when WOM:Au ratio increased from 1.4 to 14. Nevertheless, the remaining peaks from nucleobases (1250–1500 cm^{-1}) at WOM:Au = 14 and the different spectra of WOM-adsorbed DNA-Au NPs and pure WOM (in contrast to the identical spectra of AHA-adsorbed DNA-Au NPs and pure AHA in Fig. 4b) suggested that the complete shielding of ssDNA coating by WOM was unlikely. These observations are consistent with the humic nature of the WOM, which was more SRHA like. The similar long-term stability of DNA_{25}-Au and DNA_{25C}-Au in wastewater effluent was likely due to the large amount of WOM adsorbed that have weakened the role of DNA properties in controlling the colloidal stability of DNA-Au NPs.

The low ionic conditions of river water (divalent cations < 0.1 mM, conductivity = 43.5 μS/cm; Table S2) favored the suspension of DNA-Au NPs. Aggregation was not observed in the 30-min kinetics study (Fig. 7b), and approximately 80% of the particles remained suspended after 21 days (Figs. 7d and S14c), similar to their suspension in deionized water (Fig. S16). The river water organic matter (ROM, TOC = 2.3 mg C/L) shared a similar humic nature as SRHA (Fig. S15b, c). The lack of divalent cations in river water and low aromaticity of ROM suggested a weak interaction between the ROM and ssDNA coating, which was confirmed by the Raman spectra of ROM-adsorbed DNA-Au NPs, where the peak of adenine remained prominent (Fig. 7f).

3.4.2. Impact of dosed SRHA/AHA

Adding additional AHA into wastewater effluent or river water prolonged the suspension of DNA-Au NPs, and the effect of which was positively related to the dosing concentration of AHA (Figs. 7c-d and S14a and c). Such effect could be attributed to the high aromaticity of AHA compared to WOM and ROM, and the ssDNA coating preferentially adsorbed AHA molecules. The adsorption of AHA in wastewater effluent could occur via both divalent cation bridging and π-π interactions, while in river water it mainly occurred via π-π interactions.

Dosing of additional SRHA to wastewater effluent posed little impact on the colloidal stability of DNA-Au NPs (Figs. 7c and S14b) mainly due to the low aromaticity of SRHA and the already high WOM:Au ratio (14.1). As a result, the adsorption of SRHA onto DNA-Au NPs was limited and cannot to provide sufficient stabilization against the high ionic strength, particularly rich divalent cations (2.9 mM Ca^{2+} and 10 mM Mg^{2+}), of the wastewater effluent. In river water, dosing of additional SRHA at 5 mg C/L slightly enhanced the stability of DNA-Au NPs (e.g., 90% of DNA-Au NPs remained suspended after 21 days, Figs. 7d and S14d), which was a result of the substantial increased carbon-to-Au ratio (from 4.6 to 14.6). The adsorption of either SRHA or ROM was very limited due to their low aromaticity and the lack of divalent cations in river water.

Overall, these results in the real water samples highlighted the preferential interaction of ssDNA with NOM with high aromaticity, consistent with the studies in simple electrolytes. For NOM with low aromaticity, divalent cation bridging (especially by Ca^{2+}) played an essential role in their adsorption onto ssDNA.

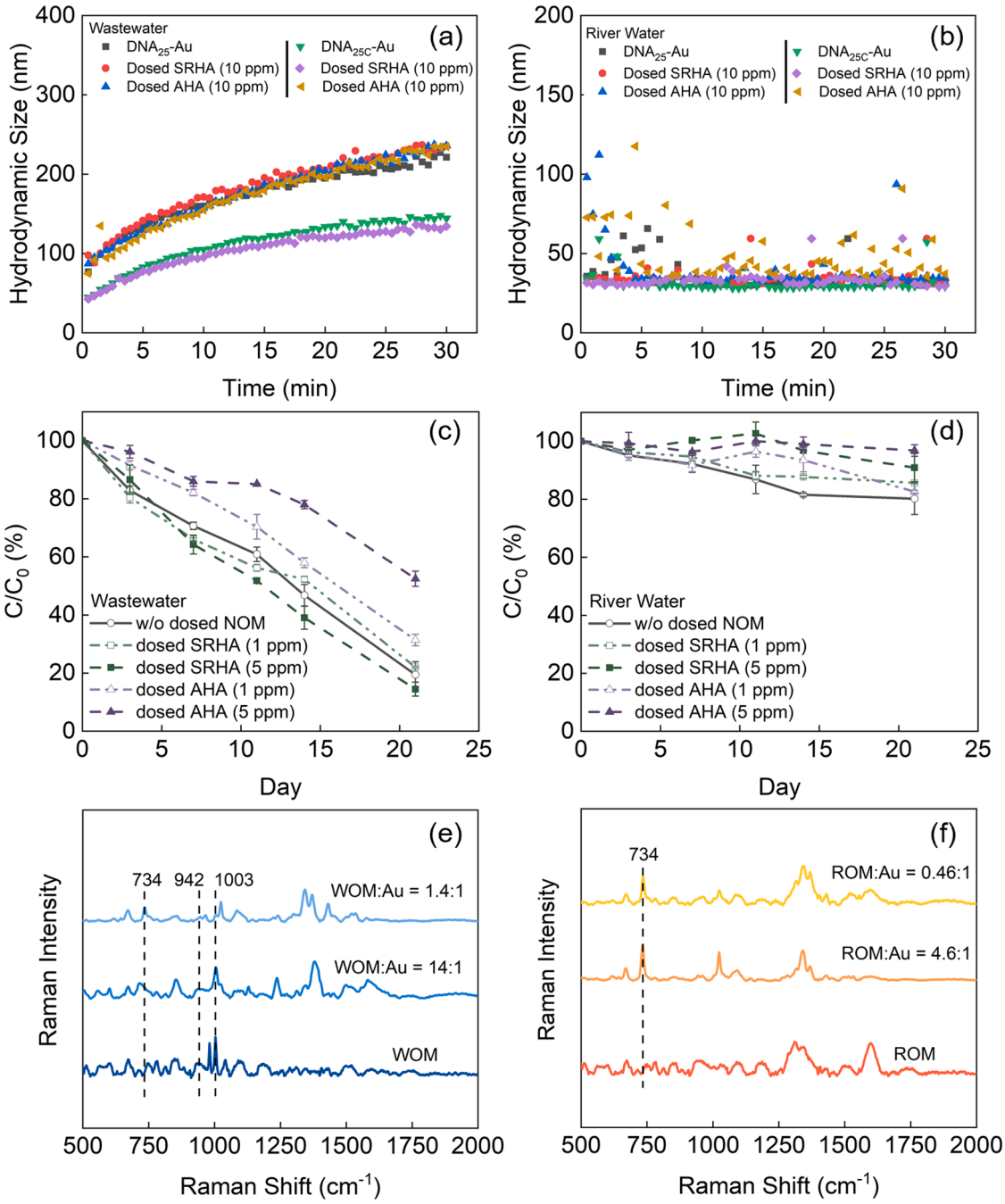

Fig. 7. (a-b) Aggregation kinetics (30-min) of DNA_{25}-Au and DNA_{25C}-Au (C_0 = 5 mg Au/L) in filtered (a) wastewater effluent and (b) river water with or without dosed SRHA or AHA (10 mg C/L). (c-d) Long-term (21-day) stability of DNA_{25}-Au (C_0 = 0.5 mg Au/L) in (c) wastewater effluent and (d) river water with or without dosed SRHA or AHA (1 or 5 mg C/L). Error bars are standard deviation of duplicates. (e-f) Raman spectra of (e) WOM-adsorbed and (f) ROM-adsorbed DNA_{25}-Au.

3.5. Implications for practical aquatic applications of engineered DNA materials

As discussed in the Introduction, interactions between NOM and engineered DNA have been reported to cause either negative or negligible influence on the performance of DNA-based applications. The observed discrepancy in literatures could possibly be induced by the difference in the carbon-to-DNA ratio (instead of NOM concentration alone), NOM properties and the subsequent (differential) interactions of NOM and DNA, as demonstrated in our earlier results. For instance, in these studies that reported no significant influence from NOM, the carbon-to-DNA ratios were around 30 and the divalent cation concentrations were low (< 1 mM) (Akki et al., 2015; Park et al., 2022). These values are considerably lower than those with which we observed significant change of the colloidal stability of DNA-Au NPs (SRHA:DNA = 1000, 4 mM Ca^{2+}, Text S5). Most noteworthy, our study revealed that the highly aromatic NOM like AHA may have the determining role in the engineered DNA functionality in typical aquatic matrices. Other less aromatic SRHA-like NOM are not likely to make the function completely fail in typical natural water chemistries. These findings have important implications for designing pretreatment strategies for terrestrial samples that may contain highly aromatic NOM. Future studies can be conducted to establish such quantitative insights.

Furthermore, our findings facilitate the general designs of aptamers and hydrological tracers for environmental applications. For aptamers, NOM (with high aromaticity) could be incorporated into the aptamer

selection process to produce aptamers with higher selectivity/binding affinity to targets, thereby improving the performance of aptasensor in real water samples. For DNA tracers, certain hydrological environments are not suitable for the use of encapsulated DNA tracers (e.g., in alluvial gravel aquifer (Pang et al., 2020)). However, adsorption of naked DNA tracers to NOM can lead to low recovery and unprecise detection (Liao et al., 2018; Pang et al., 2020). Therefore, by understanding the properties of NOM present in the field to be investigated (and other conditions such as Ca^{2+} concentrations), our work provides recommendations on whether naked DNA tracers could be directly used or certain protection to the tracers will be required.

4. Conclusions

Our study bridged the critical knowledge gap regarding the interactions between engineered short-chain ssDNA and a major natural matrix factor, i.e., NOM. The interactions between ssDNA and NOM mainly depended on the properties of NOM (i.e., carboxyl group and aromaticity), the presence of cations (i.e., valency and concentration), and the relative content of ssDNA and NOM in the system. The π-π interactions between the aromatic regions of NOM and the exposed nucleobases of ssDNA (AHA > SRHA/WOM/ROM) and the cation bridging effect (Ca^{2+} > Mg^{2+}, but not via Na^{+}) control whether the adsorbed NOM fully shield the ssDNA. With divalent cations present (specifically Ca^{2+}), even a small amount of NOM with high aromaticity (e.g., AHA) can fully shield ssDNA, whereas the extent of shielding by NOM with low aromaticity (e.g., SRHA, ROM, and WOM) depends on the relative content of ssDNA and NOM in the aquatic system and the occurrence of bridging. The extent of shielding by NOM has a major impact on the performance of engineered DNA applications, providing a partial answer to previously reported conflicting impacts of natural matrices on system performance. Overall, our findings provide new insights into the transformations of engineered ssDNA under environmentally relevant conditions, as well as implications for the rational design of engineered DNA-based environmental applications, such as selecting anti-interference aptamers and designing strategies for the protection of DNA tracers.

Declaration of Competing Interest

The authors declare that they have no known competing financial interests or personal relationships that could have appeared to influence the work reported in this paper.

Data Availability

Data will be made available on request.

Acknowledgment

The authors acknowledge partial funding support from the Guangdong-Hong Kong-Macau Joint Laboratory for Environmental Pollution and Control (K-ZGBX) and Hong Kong Research Grants Council Theme-based Research Scheme (T21-711/16-R).

Supplementary materials

Supplementary material associated with this article can be found, in the online version, at doi:10.1016/j.watres.2022.119015.

References

Abbt-Braun, G., Lankes, U., Frimmel, F.H., 2004. Structural characterization of aquatic humic substances – the need for a multiple method approach. Aquat. Sci. 66 (2), 151–170.

Akki, S.U., Werth, C.J., 2018. Critical review: DNA aptasensors, are they ready for monitoring organic pollutants in natural and treated water sources? Environ. Sci. Technol. 52 (16), 8989–9007.

Akki, S.U., Werth, C.J., Silverman, S.K., 2015. Selective aptamers for detection of estradiol and ethynylestradiol in natural waters. Environ. Sci. Technol. 49 (16), 9905–9913.

Alex, S., Dupuis, P, 1989. FT-IR and Raman investigation of cadmium binding by DNA. Inorg. Chim. Acta 157 (2), 271–281.

Chen, K.L., Elimelech, M., 2007. Influence of humic acid on the aggregation kinetics of fullerene (C60) nanoparticles in monovalent and divalent electrolyte solutions. J. Colloid Interface Sci. 309 (1), 126–134.

Chin, Y.P., Aiken, G., O'Loughlin, E., 1994. Molecular weight, polydispersity, and spectroscopic properties of aquatic humic substances. Environ. Sci. Technol. 28 (11), 1853–1858.

Coble, P.G., 1996. Characterization of marine and terrestrial DOM in seawater using excitation-emission matrix spectroscopy. Mar. Chem. 51 (4), 325–346.

Fan, L., Zhao, G., Shi, H., Liu, M., Wang, Y., Ke, H., 2014. A femtomolar level and highly selective 17β-estradiol photoelectrochemical aptasensor applied in environmental water samples analysis. Environ. Sci. Technol. 48 (10), 5754–5761.

Ghosh, S., Mashayekhi, H., Pan, B., Bhowmik, P., Xing, B., 2008. Colloidal behavior of aluminum oxide nanoparticles as affected by pH and natural organic matter. Langmuir 24 (21), 12385–12391.

Grasso, D., Chin, Y.-P., Weber, W.J., 1990. Structural and behavioral characteristics of a commercial humic acid and natural dissolved aquatic organic matter. Chemosphere 21 (10), 1181–1197.

He, S., Song, B., Li, D., Zhu, C., Qi, W., Wen, Y., Wang, L., Song, S., Fang, H., Fan, C., 2010. A graphene nanoprobe for rapid, sensitive, and multicolor fluorescent DNA analysis. Adv. Funct. Mater. 20 (3), 453–459.

Hong, S., Elimelech, M., 1997. Chemical and physical aspects of natural organic matter (NOM) fouling of nanofiltration membranes. J. Membr. Sci. 132 (2), 159–181.

Hu, X., Mu, L., Zhou, Q., Wen, J., Pawliszyn, J., 2011. ssDNA aptamer-based column for simultaneous removal of nanogram per liter level of illicit and analgesic pharmaceuticals in drinking water. Environ. Sci. Technol. 45 (11), 4890–4895.

Huangfu, X., Jiang, J., Ma, J., Liu, Y., Yang, J., 2013. Aggregation kinetics of manganese dioxide colloids in aqueous solution: influence of humic substances and biomacromolecules. Environ. Sci. Technol. 47 (18), 10285–10292.

Hur, J., Schlautman, M.A., 2003. Molecular weight fractionation of humic substances by adsorption onto minerals. J. Colloid Interface Sci. 264 (2), 313–321.

Huynh, K.A., Chen, K.L., 2011. Aggregation kinetics of citrate and polyvinylpyrrolidone coated silver nanoparticles in monovalent and divalent electrolyte solutions. Environ. Sci. Technol. 45 (13), 5564–5571.

Jiang, Y., Raliya, R., Liao, P., Biswas, P., Fortner, J.D., 2017. Graphene oxides in water: assessing stability as a function of material and natural organic matter properties. Environ. Sci.: Nano 4 (7), 1484–1493.

Kim, H.C., Yu, M.J., Han, I., 2006. Multi-method study of the characteristic chemical nature of aquatic humic substances isolated from the Han River, Korea. Appl. Geochem. 21 (7), 1226–1239.

Kim, M., Um, H.J., Bang, S., Lee, S.H., Oh, S.J., Han, J.H., Kim, K.W., Min, J., Kim, Y.H., 2009. Arsenic removal from Vietnamese groundwater using the arsenic-binding DNA aptamer. Environ. Sci. Technol. 43 (24), 9335–9340.

Korshin, G., Chow, C.W.K., Fabris, R., Drikas, M., 2009. Absorbance spectroscopy-based examination of effects of coagulation on the reactivity of fractions of natural organic matter with varying apparent molecular weights. Water Res. 43 (6), 1541–1548.

Labille, J., Thomas, F., Milas, M., Vanhaverbeke, C., 2005. Flocculation of colloidal clay by bacterial polysaccharides: effect of macromolecule charge and structure. J. Colloid Interface Sci. 284 (1), 149–156.

Liao, R., Yang, P., Wu, W., Luo, D., Yang, D., 2018. A DNA tracer system for hydrological environment investigations. Environ. Sci. Technol. 52 (4), 1695–1703.

Liu, B., Liu, J., 2017. Methods for preparing DNA-functionalized gold nanoparticles, a key reagent of bioanalytical chemistry. Anal. Methods 9 (18), 2633–2643.

Liu, B., Zhao, Y., Jia, Y., Liu, J., 2020. Heating drives DNA to hydrophobic regions while freezing drives DNA to hydrophilic regions of graphene oxide for highly robust biosensors. J. Am. Chem. Soc. 142 (34), 14702–14709.

Liu, X., Wazne, M., Chou, T., Xiao, R., Xu, S., 2011. Influence of Ca^{2+} and Suwannee river humic acid on aggregation of silicon nanoparticles in aqueous media. Water Res. 45 (1), 105–112.

Loosli, F., Le Coustumer, P., Stoll, S., 2013. TiO_2 nanoparticles aggregation and disaggregation in presence of alginate and Suwannee River humic acids. pH and concentration effects on nanoparticle stability. Water Res. 47 (16), 6052–6063.

Lu, N., Mylon, S.E., Kong, R., Bhargava, R., Zilles, J.L., Nguyen, T.H., 2012. Interactions between dissolved natural organic matter and adsorbed DNA and their effect on natural transformation of Azotobacter vinelandii. Sci. Total Environ. 426, 430–435.

Mirkin, C.A., Letsinger, R.L., Mucic, R.C., Storhoff, J.J., 1996. A DNA-based method for rationally assembling nanoparticles into macroscopic materials. Nature 382, 607–609.

Nason, J.A., McDowell, S.A., Callahan, T.W., 2012. Effects of natural organic matter type and concentration on the aggregation of citrate-stabilized gold nanoparticles. J. Environ. Monit. 14 (7), 1885–1892.

Nguyen, T.H., Chen, K.L., 2007. Role of divalent cations in plasmid DNA adsorption to natural organic matter-coated silica surface. Environ. Sci. Technol. 41 (15), 5370–5375.

Nguyen, T.H., Elimelech, M., 2007. Adsorption of plasmid DNA to a natural organic matter-coated silica surface: kinetics, conformation, and reversibility. Langmuir 23 (6), 3273–3279.

Ogram, A.V., Mathot, M.L., Harsh, J.B., Boyle, J., Pettigrew, C.A., 1994. Effects of DNA polymer length on its adsorption to soils. Appl. Environ. Microbiol. 60 (2), 393–396.

Otto, C., van den Tweel, T.J.J., de Mul, F.F.M., Greve, J., 1986. Surface-enhanced Raman spectroscopy of DNA bases. J. Raman Spectrosc. 17 (3), 289–298.
Pang, L., Abeysekera, G., Hanning, K., Premaratne, A., Robson, B., Abraham, P., Sutton, R., Hanson, C., Hadfield, J., Heiligenthal, L., Stone, D., McBeth, K., Billington, C., 2020. Water tracking in surface water, groundwater and soils using free and alginate-chitosan encapsulated synthetic DNA tracers. Water Res. 184, 116192.
Park, J., Yang, K.A., Choi, Y., Choe, J.K., 2022. Novel ssDNA aptamer-based fluorescence sensor for perfluorooctanoic acid detection in water. Environ. Int. 158, 107000.
Park, J.S., Na, H.K., Min, D.H., Kim, D.E., 2013. Desorption of single-stranded nucleic acids from graphene oxide by disruption of hydrogen bonding. Analyst 138 (6), 1745–1749.
Peng, B., Liu, Z., Jiang, Y., 2022. Aggregation of DNA-grafted nanoparticles in water: the critical role of sequence-dependent conformation of DNA coating. J. Phys. Chem. B 126 (4), 847–857.
Philippe, A., Schaumann, G.E., 2014. Interactions of dissolved organic matter with natural and engineered inorganic colloids: a review. Environ. Sci. Technol. 48 (16), 8946–8962.
Qin, C., Zhang, W., Yang, B., Chen, X., Xia, K., Gao, Y., 2018. DNA facilitates the sorption of polycyclic aromatic hydrocarbons on montmorillonites. Environ. Sci. Technol. 52 (5), 2694–2703.
Qing, Z., Zhu, L., Li, X., Yang, S., Zou, Z., Guo, J., Cao, Z., Yang, R., 2017. A target-lighted dsDNA-indicator for high-performance monitoring of mercury pollution and its antagonists screening. Environ. Sci. Technol. 51 (20), 11884–11890.
Rodríguez, F.J., Schlenger, P., García-Valverde, M., 2014. A comprehensive structural evaluation of humic substances using several fluorescence techniques before and after ozonation. Part I: Structural characterization of humic substances. Sci. Total Environ. 476-477, 718–730.
Schmid, M., Prinz, T.K., Stäbler, A., Sängerlaub, S., 2017. Effect of sodium sulfite, sodium dodecyl sulfate, and urea on the molecular interactions and properties of whey protein isolate-based films. Front. Chem. 4, 49.
Schwyzer, I., Kaegi, R., Sigg, L., Nowack, B., 2013. Colloidal stability of suspended and agglomerate structures of settled carbon nanotubes in different aqueous matrices. Water Res. 47 (12), 3910–3920.
Sierra, M.M.D., Giovanela, M., Parlanti, E., Soriano-Sierra, E.J., 2005. Fluorescence fingerprint of fulvic and humic acids from varied origins as viewed by single-scan and excitation/emission matrix techniques. Chemosphere 58 (6), 715–733.
Stankus, D.P., Lohse, S.E., Hutchison, J.E., Nason, J.A., 2011. Interactions between natural organic matter and gold nanoparticles stabilized with different organic capping agents. Environ. Sci. Technol. 45 (8), 3238–3244.
Storhoff, J.J., Lazarides, A.A., Mucic, R.C., Mirkin, C.A., Letsinger, R.L., Schatz, G.C., 2000. What controls the optical properties of DNA-linked gold nanoparticle assemblies? J. Am. Chem. Soc. 122 (19), 4640–4650.
Tsuboi, M., 1970. Application of infrared spectroscopy to structure studies of nucleic acids. Appl. Spectrosc. Rev. 3 (1), 45–90.
Vogiazi, V., de la Cruz, A.A., Varughese, E.A., Heineman, W.R., White, R.J., Dionysiou, D. D., 2021. Sensitive electrochemical detection of microcystin-LR in water samples via target-induced displacement of aptamer associated $[Ru(NH_3)_6]^{3+}$. ACS ES&T Eng. 1 (11), 1597–1605.
Yan, J., Huang, Y., Zhang, C., Fang, Z., Bai, W., Yan, M., Zhu, C., Chen, A., 2017. Aptamer based photometric assay for the antibiotic sulfadimethoxine based on the inhibition and reactivation of the peroxidase-like activity of gold nanoparticles. Microchim. Acta 184 (1), 59–63.
Yu, X., Chen, F., Wang, R., Li, Y., 2018. Whole-bacterium SELEX of DNA aptamers for rapid detection of E.coli O157:H7 using a QCM sensor. J. Biotechnol. 266, 39–49.
Zhou, J., Battig, M.R., Wang, Y., 2010. Aptamer-based molecular recognition for biosensor development. Anal. Bioanal. Chem. 398 (6), 2471–2480.